



Biomaterialization Hot Paper

How to cite: *Angew. Chem. Int. Ed.* **2021**, *60*, 18577–18581

International Edition: doi.org/10.1002/anie.202105768

German Edition: doi.org/10.1002/ange.202105768

# Intrinsically Disordered Osteopontin Fragment Orders During Interfacial Calcium Oxalate Mineralization

Hao Lu,\* David Yuen Wah Ng, Ingo Lieberwirth, Tobias Weidner, and Mischa Bonn\*

**Abstract:** Calcium oxalate ( $\text{CaC}_2\text{O}_4$ ) is the major component of kidney stone. The acidic osteopontin (OPN) protein in human urine can effectively inhibit the growth of  $\text{CaC}_2\text{O}_4$  crystals, thereby acting as a potent stone preventer. Previous studies in bulk solution all attest to the importance of binding and recognition of OPN at the  $\text{CaC}_2\text{O}_4$  mineral surface, yet molecular level insights into the active interface during  $\text{CaC}_2\text{O}_4$  mineralization are still lacking. Here, we probe the structure of the central OPN fragment and its interaction with  $\text{Ca}^{2+}$  and  $\text{CaC}_2\text{O}_4$  at the water–air interface using surface-specific non-linear vibrational spectroscopy. While OPN peptides remain largely disordered in solution, our results reveal that the bidentate binding of  $\text{Ca}^{2+}$  ions refold the interfacial peptides into well-ordered and assembled  $\beta$ -turn motifs. One critical intermediate directs mineralization by releasing structural freedom of backbone and binding side chains. These insights into the mineral interface are crucial for understanding the pathological development of kidney stones and possibly relevant for calcium oxalate biomineralization in general.

Calcium oxalate ( $\text{CaC}_2\text{O}_4$ ) is one of the most common biominerals in nature. It also occurs as an abundant organic mineral found in sediments, hydrothermal vents, and plants.<sup>[1]</sup>  $\text{CaC}_2\text{O}_4$  has three hydrated phases: calcium oxalate monohydrate (COM), calcium oxalate dehydrate (COD), and calcium oxalate trihydrate (COT). Of these, COM is the thermodynamically most stable form, and constitutes the major mineral components of kidney stone<sup>[2]</sup>—a chronic human disease affecting 10% of the population in developed countries. Due to the substantial pathological importance, different types of molecules have been applied for the inhibition of COM growth, including polyprotic acid,<sup>[2d,3]</sup> polyacid polymers<sup>[4]</sup> and peptides,<sup>[2c,e,4,5]</sup> and proteins.<sup>[2-</sup>

<sup>d,3a,b,5b,6]</sup> Much effort has been aimed at elucidating the inhibition mechanism of specific molecular functional groups,<sup>[3b–d,7]</sup> peptide sequence<sup>[5d]</sup> and its modification,<sup>[2c,5c]</sup> etc.

In the urinary system of the human body, a remarkably low concentration level of urinary proteins can effectively inhibit the growth of supersaturated  $\text{CaC}_2\text{O}_4$  crystals, thereby avoiding larger stones.<sup>[2c–e,3b,8]</sup> Understanding the mechanism underlying the biological control of those urinary proteins over  $\text{CaC}_2\text{O}_4$  mineralization is essential for developing novel therapies for kidney stone treatment. The most potent stone-inhibiting protein in urine is osteopontin (OPN). OPN features peptide domains with acidic serine and aspartate-rich motif (ASARM).<sup>[9]</sup> Previous studies in bulk solutions have shown that ASARM peptides derived from OPN are capable of inhibiting  $\text{CaC}_2\text{O}_4$  mineralization in vitro.<sup>[2c,e,10]</sup> Hoyer et al. have found that the ASARM peptides derived from the sequence 62–85 of human OPN inhibit the growth of COM crystals regardless of the phosphorylation of the serine amino acids.<sup>[2c]</sup> The authors further conclude potent inhibition requires specific charge density distribution. A similar conclusion was reached by Clark et al. in a study of the binding of protein G charge mutants to COM crystals. This study showed that the distribution of binding carboxylate groups from acidic side chains determines the binding site and orientation of the adsorbed protein.<sup>[11]</sup> Clearly, direct interactions between OPN and oxalate mineral surfaces are quintessential,<sup>[2c,d,3b,11]</sup> yet the molecular structure and interaction of OPN sequences specifically at the interfaces relevant for  $\text{CaC}_2\text{O}_4$  mineralization remain missing. Here, we show that, owing to the surface-activity of OPN, the water–air interface can be ideally used to study the OPN/ $\text{Ca}^{2+}$  binding interface as well as OPN/ $\text{CaC}_2\text{O}_4$  composite interface. While both the distribution of charge density and binding residues are affected by the folding structure of OPN protein,<sup>[12]</sup> the question arises: how is OPN folded at the above active interfaces for  $\text{CaC}_2\text{O}_4$  mineralization?

OPN protein is an intrinsically disordered protein.<sup>[13]</sup> The ASARM OPN peptides are also disordered and lack a defined (e.g.,  $\alpha$ -helical or  $\beta$ -sheet) secondary structure.<sup>[5c,14]</sup> However, the open and flexible motif for OPN allows for strong  $\text{Ca}^{2+}$  binding, which is expected to affect  $\text{CaC}_2\text{O}_4$  mineralization. To determine the structure of OPN in contact with  $\text{Ca}^{2+}$  ions, and the molecular interactions involved in  $\text{CaC}_2\text{O}_4$  mineralization, we probe the OPN-derived peptides at the interfaces with  $\text{Ca}^{2+}$  binding and within  $\text{CaC}_2\text{O}_4$  composite using surface-specific vibrational sum-frequency generation (SFG) spectroscopy. SFG has been successfully applied to probe different molecules (e.g., proteins, peptides, and water) at various interfaces.<sup>[15]</sup> The SFG experiment relies on the

[\*] Dr. H. Lu, Dr. D. Y. W. Ng, Dr. I. Lieberwirth, Prof. M. Bonn  
Department of Molecular Spectroscopy  
Max Planck Institute for Polymer Research  
Ackermannweg 10, 55128 Mainz (Germany)  
E-mail: lu@mpip-mainz.mpg.de  
bonn@mpip-mainz.mpg.de

Prof. T. Weidner  
Department of Chemistry, Aarhus University  
Langelandsgade 140, 8000 Aarhus C (Denmark)

Supporting information and the ORCID identification number(s) for the author(s) of this article can be found under:  
<https://doi.org/10.1002/anie.202105768>.

© 2021 The Authors. Angewandte Chemie International Edition published by Wiley-VCH GmbH. This is an open access article under the terms of the Creative Commons Attribution License, which permits use, distribution and reproduction in any medium, provided the original work is properly cited.

frequency mixing of infrared (IR) and visible laser pulses. Molecular resonances excited by the IR pulse enhance the signal and yield a vibrational spectrum of interfacial molecules. The selection rules dictate that SFG signals can only be generated from ordered interfacial molecules for which, on average, centrosymmetry is broken.<sup>[16]</sup> As such, SFG is well suitable to probe the structure and interaction of OPN molecules, specifically at the interface and *in situ*. Here, we investigate a representative ASARM peptide derived from region 62–85 of human OPN (H<sub>2</sub>NSNESHDMDDMDEDDDDHVDSDCOOH), abbreviated as OPN peptide below.

Before focusing OPN peptides at the interface, we first perform CD measurements (180–260 nm) to determine the secondary structure content of unbound OPN peptides in bulk water and potential changes when adding Ca<sup>2+</sup> and subsequently C<sub>2</sub>O<sub>4</sub><sup>2-</sup> for CaC<sub>2</sub>O<sub>4</sub> mineralization. As seen in Figure 1 a, the CD spectra of OPN peptides all exhibit one dominant negative ellipticity at 200 nm and a small secondary

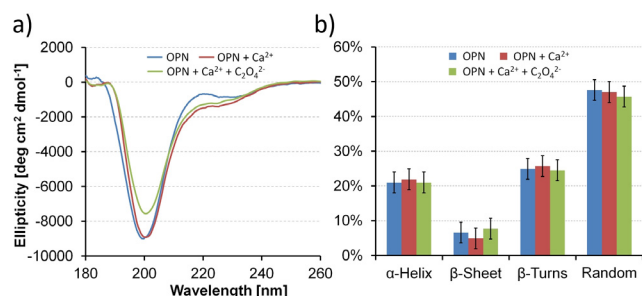


**Figure 1.** a) Circular dichroism spectra of OPN peptides in water solution (blue), with addition of Ca<sup>2+</sup> cations (red) and subsequently C<sub>2</sub>O<sub>4</sub><sup>2-</sup> anions for CaC<sub>2</sub>O<sub>4</sub> mineralization (green). b) Secondary structure estimation of the respective OPN peptides in water solution (blue), with addition of Ca<sup>2+</sup> cations (red), and subsequently C<sub>2</sub>O<sub>4</sub><sup>2-</sup> anions (green).

band at 230 nm. These two bands correspond to the  $\pi$ - $\pi^*$  and  $n$ - $\pi^*$  transition of the amide bond, respectively.<sup>[17]</sup> In agreement with studies on disordered oligopeptides, the signatures reflect a major contribution from random coils and  $\beta$ -turns,<sup>[18]</sup> while lacking in defined secondary structures such as  $\alpha$ -helix or  $\beta$ -sheet. The structure inferred from CD measurement is in good agreement with previous studies on OPN peptides.<sup>[5c,14]</sup> Multivariate secondary structure analysis was performed using the partial least squares method fitted against standard proteins (i.e., lysozyme, cytochrome *c*) within the JASCO library.<sup>[19]</sup> The secondary structures remain essentially unchanged upon adding Ca<sup>2+</sup> and subsequently C<sub>2</sub>O<sub>4</sub><sup>2-</sup> ions. A secondary structure analysis shown in Figure 1b reveals approximately 21%  $\alpha$ -helix, 7%  $\beta$ -sheet, 25%  $\beta$ -turns, and 47% random coils.

The secondary structure for OPN peptides in solution does not necessarily represent their structure at the interface. Figure 2 illustrates our strategy tackling OPN structure at the interface during CaC<sub>2</sub>O<sub>4</sub> mineralization: The peptides were firstly allowed to adsorb at the air–water interface (top panel). The peptides at the air–water interface provide an ideal two-dimensional “soft” interface,<sup>[20]</sup> allowing us to study

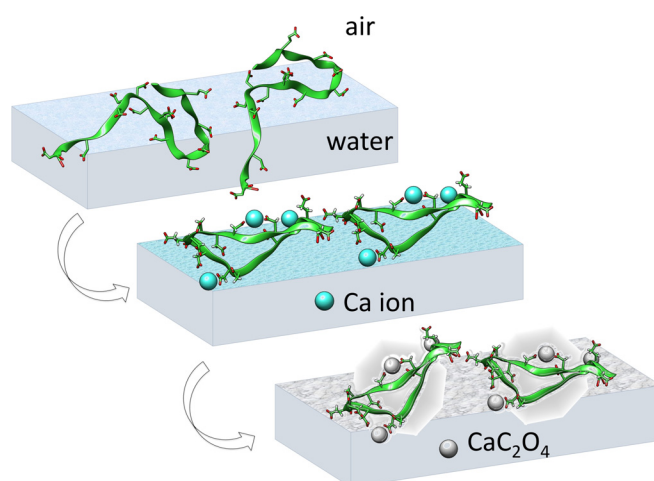


**Figure 2.** Scheme illustrating the OPN peptides at the air–solution interface (top), with Ca<sup>2+</sup> ions (middle), and CaC<sub>2</sub>O<sub>4</sub> minerals (bottom). Initially, OPN peptides are disordered at the air–water interface (top), but will refold into an ordered  $\beta$ -turn structure upon interfacial binding to Ca<sup>2+</sup> (middle) and CaC<sub>2</sub>O<sub>4</sub> minerals (bottom). The OPN peptides show dynamic features in the solution during the simulation. The depicted structures are generated from simulation frames to illustrate the interaction-induced ordering at the interface.

the interfacial interaction of OPN peptides with Ca<sup>2+</sup> ions and further CaC<sub>2</sub>O<sub>4</sub> minerals. Adding Ca<sup>2+</sup> cations is expected to bind and refold interfacial peptides (middle panel). The subsequent addition of C<sub>2</sub>O<sub>4</sub><sup>2-</sup> anions will initiate interfacial mineralization within refolded peptides (bottom panel). Surface pressure measurements show that the adsorbed peptides reach a surface pressure of 25 mN m<sup>-1</sup>. The surface pressure decreases only slightly with the addition of Ca<sup>2+</sup> and C<sub>2</sub>O<sub>4</sub><sup>2-</sup> ions, suggesting the nearly constant density of interfacial peptides throughout the mineralization process (Figure S1).

Interfacial mineralization is expected to complete within 20 minutes after injecting C<sub>2</sub>O<sub>4</sub><sup>2-</sup> anions.<sup>[21]</sup> A thin nanosheet consisting of CaC<sub>2</sub>O<sub>4</sub> minerals and OPN peptides can be lifted off the interface with a transmission electron microscopy (TEM) grid using the Langmuir–Schaefer approach.<sup>[21a]</sup> CaC<sub>2</sub>O<sub>4</sub> mineralization by peptides in solution has been extensively reported, while interfacial mineralization, resulting in a peptide/CaC<sub>2</sub>O<sub>4</sub> composite, has not been well studied.<sup>[21a]</sup> We applied TEM and X-ray photoelectron spectroscopy (XPS) to characterize the obtained interfacial nanosheet composites. Figure 3a shows the TEM image of the nanosheet, intact over micrometers. The obtained thin peptide–oxalate nanosheet provides an ideal platform to study interfacial CaC<sub>2</sub>O<sub>4</sub> mineralization by OPN peptides. The chemical composition of the composite nanosheet was confirmed by XPS: distinct Ca2p and N1s emission peaks (Figure S2) indicate the presence of peptides and oxalate minerals. The high-resolution TEM image in Figure 3b highlights the nanocrystalline CaC<sub>2</sub>O<sub>4</sub> particles within the sheet. The obtained nanocrystals indicate that OPN peptides are highly efficient nucleators for interfacial mineralization. The exact crystal composition (e.g., COM or COD) could not be well determined from diffraction measurements, which

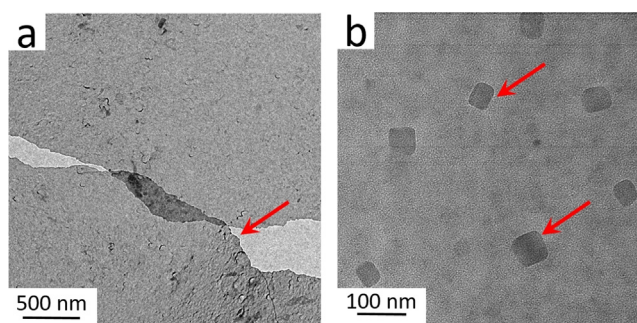


**Figure 3.** a) TEM image showing the nanosheet composed of OPN peptides and  $\text{CaC}_2\text{O}_4$  minerals. The red arrow marks the ruptured film. b) High-resolution TEM image of the crystalline  $\text{CaC}_2\text{O}_4$  mineral nanocrystals within the nanosheet. The red arrows highlight  $\text{CaC}_2\text{O}_4$  crystals.

may be caused by the crystal decomposition as induced by the high-energy electron beam.<sup>[22]</sup> We further examine the  $\text{CaC}_2\text{O}_4$  crystals by OPN peptides in bulk solution; the tetragonal morphology and diffraction analysis indicate COD crystals are obtained (Figure S3).

To glean molecular-level insights into OPN peptides when mineralizing an interface, we applied surface-specific SFG spectroscopy. SFG selectively probes the outermost approximately 2 nm of the water surface, allowing to probe interfacial peptides without contribution from peptide molecules in bulk solution. Figure 4a shows SFG spectra in the CH/OH region for OPN peptides adsorbed at the air–water interface, with  $\text{Ca}^{2+}$  ion interaction and further  $\text{CaC}_2\text{O}_4$  mineralization. The CH bands appear at  $2878\text{ cm}^{-1}$  and  $2950\text{ cm}^{-1}$ , corresponding to the symmetric  $\text{CH}_3$  stretch, and a combination of  $\text{CH}_3$  Fermi resonance and  $\text{CH}_2$  stretch from different amino acid side chains, respectively.<sup>[23]</sup> The water response gives rise to two broad OH stretch bands centered at  $3241\text{ cm}^{-1}$  and  $3410\text{ cm}^{-1}$ , with an overall first moment centered at  $3276\text{ cm}^{-1}$ , indicating the presence of strongly and weakly hydrogen-bonded water molecules.<sup>[15c,24]</sup> The OH response is rather intense, owing to the negatively charged peptides, which align the water dipoles and thereby break centrosymmetry within the interfacial water layers. The OH response decreases with adding  $\text{Ca}^{2+}$  ions, implying decreased water alignment; the first moment value increases by  $63\text{ cm}^{-1}$  (from  $3276$  to  $3339\text{ cm}^{-1}$ ), suggesting weakening of the hydrogen bond strength. The observed change in OH bands is mainly due to  $\text{Ca}^{2+}$  ions, which interact at the OPN interface and screen the peptide charge, thereby modifying the structure of interfacial water. No obvious spectral change is observed during  $\text{CaC}_2\text{O}_4$  mineralization.

The substantial perturbation of the peptide hydration shell prompts us to look closely at the interfacial peptides. To this end, we record SFG spectra in the amide I region, for SSP (S-polarized SFG and Vis, P-polarized IR) and SPS (S-polarized SFG, P-polarized Vis, S-polarized IR) polarization combinations, as shown in Figure 4b,c. Both spectra for original OPN peptides show nearly zero signal, suggesting a complete lack of peptide order, consistent with the intrinsically disordered motif of OPN in bulk solution from CD measurement. When adding  $\text{Ca}^{2+}$  ions, the SSP spectra exhibit

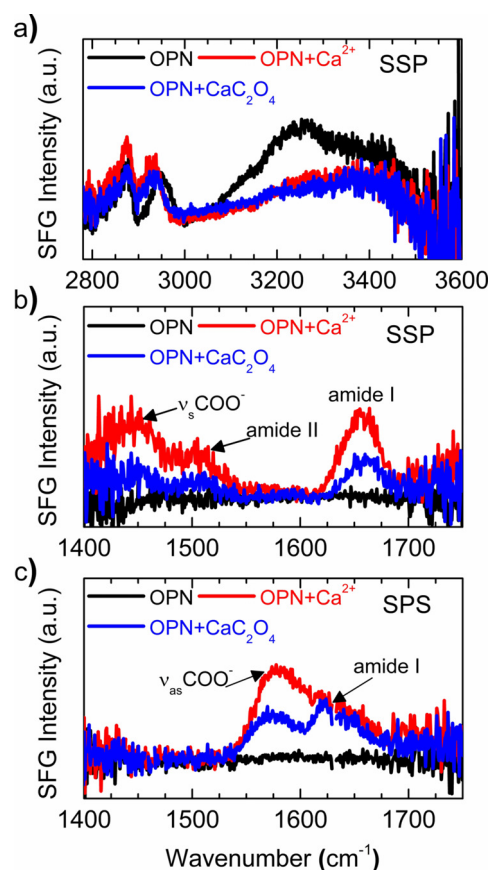


**Figure 4.** SFG spectra in CH/OH (a) and amide I region (b,c) for OPN peptides adsorbed at the air–water interface (black), with  $\text{Ca}^{2+}$  ion interaction (red), and further  $\text{CaC}_2\text{O}_4$  mineralization (blue). The spectra were acquired under SSP (a,b) and SPS (c) polarization combinations.

three distinct SFG bands: one side chain band at circa  $1447\text{ cm}^{-1}$ , attributed to symmetric  $\text{COO}^-$  stretch from the deprotonated acidic side-chains (e.g. of glutamic and aspartic acid); and two backbone bands at approximately  $1507\text{ cm}^{-1}$  and  $1652\text{ cm}^{-1}$ , assigned to amide II and amide I bands, respectively. Similarly, the SPS spectra in Figure 4c reveal two dominating bands for peptides with  $\text{Ca}^{2+}$ : one at approximately  $1570\text{ cm}^{-1}$  from the asymmetric  $\text{COO}^-$  stretch of the deprotonated acidic side-chains and another at approximately  $1611\text{ cm}^{-1}$  for backbone amide I mode. Apparently, as sketched in Figure 2, the binding of  $\text{Ca}^{2+}$  ions restructures the peptide backbone and binding side chains from a disordered into a well-ordered motif. Following interfacial  $\text{CaC}_2\text{O}_4$  mineralization, this order diminishes somewhat, as revealed by the reduced intensities of the SFG peaks.

The resonance frequency of the side-chain mode is sensitive to the  $\text{COO}-\text{Ca}$  binding geometry, and the observed frequency of circa  $1570\text{ cm}^{-1}$  reveals bidentate binding.<sup>[21a]</sup> The well-coordinated  $\text{Ca}^{2+}$  ions refold the disordered backbone into a defined secondary structure, as evidenced by the distinct amide I peaks. The fitting frequencies at  $1652\text{ cm}^{-1}$  in SSP spectra and  $1611\text{ cm}^{-1}$  in SPS spectra (Table S1 and S2), together with comparing analogous spectra for leucine–glutamic acid sequences (Figure S5), suggest the  $\beta$ -turn secondary structure,<sup>[12a,21a,25]</sup> which is in agreement with

previous simulation studies for OPN sequences binding at the  $\text{CaC}_2\text{O}_4$  mineral surface.<sup>[14,26]</sup> Interestingly, the amide II band is also well discernible in the SSP spectra (Figure 4b). The amide II mode arises from the out-of-phase combination of the C–N stretch and the N–H in-plane deformation.<sup>[27]</sup> It is Raman inactive,<sup>[28]</sup> and, therefore, in principle, not SFG-detectable since the SFG signal is proportional to a tensor product of the IR transition dipole moment and the Raman polarizability.<sup>[16]</sup> However, recent studies have shown that amide II modes can be visible in SFG spectra for folding motifs with extended tertiary structure (e.g. multi-stranded  $\beta$ -sheets), where the long-range vibrational coupling from intermolecular  $\beta$ -sheet contacts can enhance the amide II signals.<sup>[29]</sup> Here the observable amide II band suggests the assembly of well-aligned  $\beta$ -turn peptides, as caused by the intercalating  $\text{Ca}^{2+}$  ions. The ordered peptide assemblies may act as a critical structural intermediate that guides interfacial mineralization, resulting in 2D-nanosheet-containing crystalline minerals (Figure 3). The assembled peptides can also be fingerprinted in high-resolution TEM imaging (Figure S4). During mineralization, the consumption of coordinated  $\text{Ca}^{2+}$  ions by  $\text{C}_2\text{O}_4^{2-}$  breaks the bidentate binding and results in the decreased order in both backbone and side chains. Interestingly, the concentration of OPN peptides in solution is 17.7 nM, which is below physiological conditions; adding  $\text{Ca}^{2+}$  and subsequent  $\text{C}_2\text{O}_4^{2-}$  ions in a higher mM range will not change the structure of free peptides in solution, but rather refold interfacial peptides into a well-defined  $\beta$ -turn motif.

In conclusion, we have applied surface-specific SFG spectroscopy to probe the structure of the central OPN fragment, its interaction with  $\text{Ca}^{2+}$ , and  $\text{CaC}_2\text{O}_4$  mineralization. Contrary to the unchanged disordered structure in bulk solution, we show that the bidentate interaction with  $\text{Ca}^{2+}$  ions refolds the OPN peptides into a well-ordered and assembled  $\beta$ -turn motif at the OPN-covered aqueous  $\text{Ca}^{2+}$  solution surface, where interfacial mineralization can subsequently occur. Our results highlight the significantly different behavior of OPN peptides at the interface and in bulk solution for  $\text{CaC}_2\text{O}_4$  mineralization. In particular, the critical peptide– $\text{Ca}^{2+}$  binding interface should be taken into account in  $\text{CaC}_2\text{O}_4$  mineralization, for example, for the treatment of kidney stones; such interfacial processes may also be relevant for calcium phosphate biomineralization in bone formation.

## Acknowledgements

The authors thank Katrin Kirchhoff for TEM measurements. We are greatly indebted to Sarah Alamdari and Prof. Jim Pfaendtner for their initial efforts in MD simulations and Dr. Steven J. Roeters for SFG spectra calculation from MD simulated structures. Open access funding enabled and organized by Projekt DEAL.

## Conflict of Interest

The authors declare no conflict of interest.

**Keywords:** calcium oxalate mineralization · interface · kidney stone · osteopontin · sum-frequency generation spectroscopy

- [1] T. Echigo, M. Kimata, *Can. Mineral.* **2010**, *48*, 1329–1357.
- [2] a) R. L. Ryall, *World J. Urol.* **1997**, *15*, 155–164; b) F. L. Coe, A. Evan, E. Worcester, *J. Clin. Invest.* **2005**, *115*, 2598–2608; c) J. R. Hoyer, J. R. Asplin, L. Otvos, *Kidney Int.* **2001**, *60*, 77–82; d) S. R. Qiu, A. Wierzbicki, C. A. Orme, A. M. Cody, J. R. Hoyer, G. H. Nancollas, S. Zepeda, J. J. De Yoreo, *Proc. Natl. Acad. Sci. USA* **2004**, *101*, 1811–1815; e) Y. C. Chien, D. L. Masica, J. J. Gray, S. Nguyen, H. Vali, M. D. Mckee, *J. Biol. Chem.* **2009**, *284*, 23491–23501.
- [3] a) J. J. De Yoreo, S. R. Qiu, J. R. Hoyer, *Am. J. Physiol. Renal Physiol.* **2006**, *291*, F1123–F1131; b) X. X. Sheng, T. S. Jung, J. A. Wesson, M. D. Ward, *Proc. Natl. Acad. Sci. USA* **2005**, *102*, 267–272; c) J. Chung, R. Sosa, J. D. Rimer, *Cryst. Growth Des.* **2017**, *17*, 4280–4288; d) J. Chung, M. G. Taylor, I. Granja, J. R. Asplin, G. Mpourmpakis, J. D. Rimer, *Cryst. Growth Des.* **2018**, *18*, 5617–5627.
- [4] T. Jung, X. X. Sheng, C. K. Choi, W. S. Kim, J. A. Wesson, M. D. Ward, *Langmuir* **2004**, *20*, 8587–8596.
- [5] a) S. W. Guo, M. D. Ward, J. A. Wesson, *Langmuir* **2002**, *18*, 4284–4291; b) A. A. Campbell, A. Ebrahimpour, L. Perez, S. A. Smesko, G. H. Nancollas, *Calcif. Tissue Int.* **1989**, *45*, 122–128; c) L. J. Wang, X. Y. Guan, R. K. Tang, J. R. Hoyer, A. Wierzbicki, J. J. De Yoreo, G. H. Nancollas, *J. Phys. Chem. B* **2008**, *112*, 9151–9157; d) L. J. Wang, S. R. Qiu, W. Zachowicz, X. Y. Guan, J. J. De Yoreo, G. H. Nancollas, J. R. Hoyer, *Langmuir* **2006**, *22*, 7279–7285.
- [6] a) S. Farmanesh, S. Ramamoorthy, J. H. Chung, J. R. Asplin, P. Karande, J. D. Rimer, *J. Am. Chem. Soc.* **2014**, *136*, 367–376; b) S. Farmanesh, J. H. Chung, R. D. Sosa, J. H. Kwak, P. Karande, J. D. Rimer, *J. Am. Chem. Soc.* **2014**, *136*, 12648–12657.
- [7] X. X. Sheng, M. D. Ward, J. A. Wesson, *J. Am. Chem. Soc.* **2003**, *125*, 2854–2855.
- [8] B. Grohe, J. O'Young, D. A. Ionescu, G. Lajoie, K. A. Rogers, M. Karttunen, H. A. Goldberg, G. K. Hunter, *J. Am. Chem. Soc.* **2007**, *129*, 14946–14951.
- [9] S. G. Liu, P. S. N. Rowe, L. Vierthaler, J. P. Zhou, L. D. Quarles, *J. Endocrinol.* **2007**, *192*, 261–267.
- [10] Y. Liu, H. Y. Mao, X. F. Liu, L. J. Qiao, R. Guo, *CrystEngComm* **2014**, *16*, 8841–8851.
- [11] R. H. Clark, A. A. Campbell, L. A. Klumb, C. J. Long, P. S. Stayton, *Calcif. Tissue Int.* **1999**, *64*, 516–521.
- [12] a) H. Lu, H. Lutz, S. J. Roeters, M. A. Hood, A. Schafer, R. Munoz-Espi, R. Berger, M. Bonn, T. Weidner, *J. Am. Chem. Soc.* **2018**, *140*, 2793–2796; b) J. E. Baio, A. Zane, V. Jaeger, A. M. Roehrich, H. Lutz, J. Pfaendtner, G. P. Drobny, T. Weidner, *J. Am. Chem. Soc.* **2014**, *136*, 15134–15137.
- [13] D. Kurzbach, G. Platzer, T. C. Schwarz, M. A. Henen, R. Konrat, D. Hinderberger, *Biochemistry* **2013**, *52*, 5167–5175.
- [14] P. V. Azzopardi, J. O'Young, G. Lajoie, M. Karttunen, H. A. Goldberg, G. K. Hunter, *PLoS One* **2010**, *5*, e9330.
- [15] a) S. Roy, P. A. Covert, W. R. FitzGerald, D. K. Hore, *Chem. Rev.* **2014**, *114*, 8388–8415; b) B. Ding, J. Jasensky, Y. Li, Z. Chen, *Acc. Chem. Res.* **2016**, *49*, 1149–1157; c) M. Bonn, Y. Nagata, E. H. G. Backus, *Angew. Chem. Int. Ed.* **2015**, *54*, 5560–5576; *Angew. Chem.* **2015**, *127*, 5652–5669.
- [16] a) Y. R. Shen, *The Principles of Nonlinear Optics*, Wiley, New York, **1984**; b) A. G. Lambert, P. B. Davies, D. J. Neivandt, *Appl. Spectrosc. Rev.* **2005**, *40*, 103–145.
- [17] C. A. Bush, S. K. Sankar, K. D. Kopple, *Biochemistry* **1978**, *17*, 4951–4954.

- [18] a) P. F. J. Fuchs, A. M. J. J. Bonvin, B. Bochicchio, A. Pepe, A. J. P. Alix, A. M. Tamburro, *Biophys. J.* **2006**, *90*, 2745–2759; b) L. B. Chemes, L. G. Alonso, M. G. Noval, G. de Prat-Gay, *Methods Mol. Biol.* **2012**, *895*, 387–404.
- [19] W. C. Johnson, *Proteins Struct. Funct. Bioinf.* **1999**, *35*, 307–312.
- [20] a) D. C. Popescu, M. M. J. Smulders, B. P. Pichon, N. Chebotarova, S. Y. Kwak, O. L. J. van Asselen, R. P. Sijbesma, E. DiMasi, N. A. J. M. Sommerdijk, *J. Am. Chem. Soc.* **2007**, *129*, 14058–14067; b) S. Cavalli, D. C. Popescu, E. E. Tellers, M. R. J. Vos, B. P. Pichon, M. Overhand, H. Rapaport, N. A. J. M. Sommerdijk, A. Kros, *Angew. Chem. Int. Ed.* **2006**, *45*, 739–744; *Angew. Chem.* **2006**, *118*, 753–758.
- [21] a) H. Lu, A. Schafer, H. Lutz, S. J. Roeters, I. Lieberwirth, R. Munoz-Espi, M. A. Hood, M. Bonn, T. Weidner, *J. Phys. Chem. Lett.* **2019**, *10*, 2170–2174; b) V. Fischer, K. Landfester, R. Muñoz-Espí, *Cryst. Growth Des.* **2011**, *11*, 1880–1890.
- [22] E. Ruiz-Agudo, A. Burgos-Cara, C. Ruiz-Agudo, A. Ibanez-Velasco, H. Colfen, C. Rodriguez-Navarro, *Nat. Commun.* **2017**, *8*, 768.
- [23] a) M. R. Watry, G. L. Richmond, *J. Phys. Chem. B* **2002**, *106*, 12517–12523; b) G. J. Holinga, R. L. York, R. M. Onorato, C. M. Thompson, N. E. Webb, A. P. Yoon, G. A. Somorjai, *J. Am. Chem. Soc.* **2011**, *133*, 6243–6253.
- [24] Q. Du, E. Freysz, Y. R. Shen, *Science* **1994**, *264*, 826–828.
- [25] a) K. T. Nguyen, J. T. King, Z. Chen, *J. Phys. Chem. B* **2010**, *114*, 8291–8300; b) B. R. Singh, *Infrared Analysis of Peptides and Proteins: Principles and Applications*, American Chemical Society, Washington, DC, **2000**.
- [26] G. K. Hunter, J. O'Young, B. Grohe, M. Karttunen, H. A. Goldberg, *Langmuir* **2010**, *26*, 18639–18646.
- [27] A. Barth, C. Zscherp, *Q. Rev. Biophys.* **2002**, *35*, 369–430.
- [28] S. Krimm, J. Bandekar, *Adv. Protein Chem.* **1986**, *38*, 181–364.
- [29] a) J. J. Tan, J. H. Zhang, Y. Luo, S. J. Ye, *J. Am. Chem. Soc.* **2019**, *141*, 1941–1948; b) L. Fu, D. Q. Xiao, Z. G. Wang, V. S. Batista, E. C. Y. Yan, *J. Am. Chem. Soc.* **2013**, *135*, 3592–3598.

Manuscript received: April 28, 2021

Revised manuscript received: May 19, 2021

Accepted manuscript online: June 12, 2021

Version of record online: July 16, 2021